ROYAL SOCIETY
OF CHEMISTRY

PAPER

CrossMark
click for updates

Tunable auto-combustion preparation of TiO₂ nanostructures as efficient adsorbents for the removal of an anionic textile dye†

Mostafa Y. Nassar,*[a] Eman I. Ali[a] and Essam S. Zakaria[b]

We have developed a new route for the synthesis of pure TiO₂ nanostructures *via* a facile auto-combustion method followed by heat treatment. We have tuned the produced phases, morphologies, and crystallite sizes of the nano-sized TiO₂ products through an auto-combustion method employing different fuels and various fuel-to-oxidant equivalence ratios, Φ_c. The as-synthesized products were analyzed by means of FE-SEM, FT-IR, XRD, TEM, BET, and thermal analyses. Interestingly, urea fuel at $\Phi_c = 1$ generated a pure anatase TiO₂ phase (U1) having almost the smallest crystallite size (11.9 nm) and the highest adsorption capacity (135 mg g⁻¹) for the removal of Reactive Red 195 (RR195) dye from aqueous solutions. Moreover, the adsorption data could be described well using the pseudo-second-order kinetic and Langmuir isotherm models. Based on the calculated thermodynamic parameters: ΔH^0 (1.343 kJ mol⁻¹), ΔG^0 (from −4.630 to −5.031 kJ mol⁻¹), and E_a (18.46 kJ mol⁻¹), the adsorption of RR195 dye on the as-prepared TiO₂ nano-adsorbent is an endothermic, spontaneous, and physisorption process, respectively. Moreover, the as-prepared TiO₂ adsorbent is a promising candidate for the removal of RR195 textile dye from aqueous media based on its reusability, high stability, and high adsorption capacity.

1. Introduction

Because of the environmental problems that water pollution may cause, a great number of researchers have devoted their efforts to the wastewater treatment research field. One of the serious sources of water pollution is the dying processing included in various industries such as paper, leather, plastic, rubber, and textile. These industries discharge large quantities of organic dyes into the water environment without pre-treatment.[1–3] The discharged dyes, including reactive red dye, are non-biodegradable and chemically stable. In addition, these dyes are toxic and carcinogenic owing to the presence of azo groups (–N═N–) in their molecular structures.[4] Besides, these dyes cause serious problems to human health such as irritation, respiratory issues chemical burns, ulcers, *etc.*[5,6] Hence, the removal of the organic dyes (especially the textile dyes) from wastewaters is one of the critical necessities for human and environmental safety.

To date, physical, chemical, and biological methods have been proposed for the removal of the dyes from wastewaters. Therefore, several methods have been suggested for this purpose such as membrane separation, coagulation, ultra-sonication, photocatalysis, ozonation, biological treatment, and adsorption.[7–14] Among these methods, adsorption was considered to be one of the most efficient techniques for the removal of non-biodegradable contaminants from wastewater owing to its simplicity in operation, high efficiency, economic applicability, scalability, and the availability of numerous adsorbents.[15,16] In this vein, various adsorbent materials including natural and synthesized polymers, zeolites, activated carbons, hydrotalcites, and clays have been proposed for treatment of wastewater from textile dyes.[1,17–19]

Recently, various research groups have devoted their effort to searching for adsorbents with high surface areas, low-cost production, and non-toxic characteristics to the environment. The scientists found their way in nano-sized materials which have been regarded as an important type of adsorbent materials for the removal of heavy metals and organic pollutants from wastewater.[2,4,20–23] However, reports on the removal of Reactive Red 195 (RR195) dye from wastewater are still limited.[2,20] Besides, searching for the most suitable nano-adsorbent is still a challenge.

Meanwhile, titanium oxide and its composite nanostructures have been proved their efficiency as nano-adsorbents and/or nano-catalysts for the removal of some dyes from wastewater.[24,25] So far, various methods have been developed for preparing TiO₂ nanostructures such as hydrothermal,[26,27] anodic oxidation,[28] electrodeposition,[29,30] microwave,[31] sol–gel,[27,32] chemical vapor deposition (CVD),[33] and combustion methods.[34,35] Among these methods, combustion route has

[a]Chemistry Department, Faculty of Science, Benha University, Benha 13518, Egypt. E-mail: m_y_nassar@yahoo.com; m_y_nassar@fsc.bu.edu; Tel: +20 1068727555

[b]Hot Laboratories Center, Atomic Energy Authority, P.O. Box 13759, Cairo, Egypt

† Electronic supplementary information (ESI) available. See DOI: 10.1039/c6ra27924d

This journal is © The Royal Society of Chemistry 2017

been considered as one of the most efficient routes due to its low-cost production and scalability. However, reports on combustion synthesis of TiO$_2$ nanoparticles are limited.[34,35] In addition, combustion synthesis of titanium oxide nano-structures using TiCl$_4$ precursor, tuning the produced TiO$_2$ phase, and employing the produced TiO$_2$ nanostructure as an adsorbent for the removal of Reactive Red 195 (RR195) dye have not been reported so far, to the best of our knowledge.

Therefore, in the present work, we report a facile auto-combustion synthesis of TiO$_2$ nanostructures using a relatively inexpensive TiCl$_4$ precursor, for the first time. The effect of the fuel type and fuel-to-oxidant equivalence ratio on the particle size, morphology, and produced TiO$_2$ phase nano-structures were explored. The products were characterized using various spectroscopic tools. Investigation of the adsorption properties of the products showed high adsorption capacity of the as-synthesized TiO$_2$ nanoparticles for the removal of Reactive Red 195 (RR195) dye (Scheme S1, ESI†), as an anionic textile dye. The kinetics and thermodynamics of the adsorption process, as well as the recyclability of the nano-adsorbent, were studied.

2. Experimental

2.1. Materials and reagents

Titanium tetrachloride (TiCl$_4$), potassium chloride (KCl), sodium chloride (NaCl), urea (NH$_2$CONH$_2$), glycine (NH$_2$CH$_2$-COOH), L-alanine (CH$_3$CH(NH$_2$)COOH), and TiO$_2$ nanopowder (Degussa (P25)) were supplied by Sigma-Aldrich Company. Nitric acid (HNO$_3$) was provided from Carlo Erba Company, France. Reactive Red 195 dye (RR195) (C$_{31}$H$_{19}$ClN$_7$O$_{19}$S$_6$Na$_5$; Scheme S1, ESI†) was purchased from Rushabh chemicals industries, India. All other reagents and chemicals were of analytical grade and employed as received without further purification.
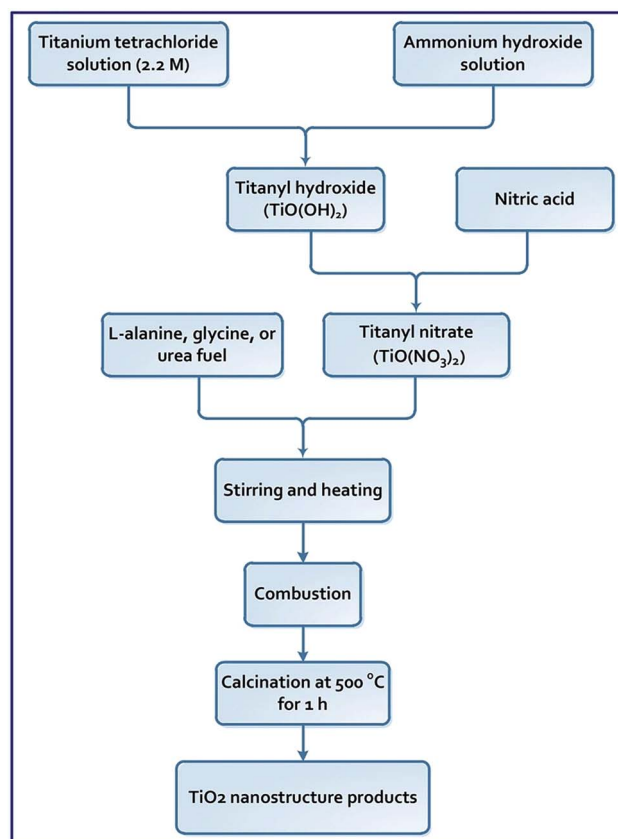
2.2. Synthesis of TiO$_2$ nanostructures using different fuels

An auto-combustion method was developed to synthesize TiO$_2$ nanoparticles utilizing three different fuels: L-alanine, glycine, and urea. The produced TiO$_2$ samples are referred to as A, G, and U, respectively. Notably, for the combustion process, the stoichiometric compositions of the redox blends are calculated according to that the total reducing (F) and oxidizing (O) valencies of the fuel and TiO(NO$_3$)$_2$, respectively, verify that Φ_c = (F/O) = 0.5, 1, 1.5, 2, and 2.5 (where, Φ_c is the equivalence ratio).[8,36] Titanium chloride aqueous solution of a concentration of 2.2 M was prepared by diluting the purchased titanium tetrachloride (TiCl$_4$) in cold HCl aqueous solution (4 M) under nitrogen gas atmosphere. The prepared 2.2 M titanium chloride solution was employed in the subsequent experiments. In a typical experiment: 10 mL of 2.2 M titanium chloride solution (22 mmol, 10 eq.) was diluted in cold bi-distilled water (100 mL). An aqueous ammonium hydroxide solution was then added slowly to a vigorously stirring and cold titanium chloride solution until pH reached 8.5. During this step, white precipitate of TiO(OH)$_2$ was formed. The precipitate (TiO(OH)$_2$) was collected by centrifugation, washed with water, and converted into *in situ* titanyl nitrate solution (TiO(NO$_3$)$_2$) by adding the least amount of concentrated nitric acid to the white suspension and letting the reaction blend stir at room temperature for 1 h. Solid urea (2.2 g, 36.67 mmol, 6 eq.), as fuel, was added to the titanyl nitrate solution and stirred for 10 min for complete dissolution. In this example, this quantity of the fuel was added so that the calculated Φ_c was maintained at 1 (*i.e.* (F/O) = 1). The auto-combustion process was then performed on a hot plate at about 300 °C for 10 min. The produced yellowish precursor was grounded and calcined in a muffle at 500 °C for 1 h to give TiO$_2$ product referred to as U1. Similar experiments were repeated while different quantities of urea were used to have different Φ_c = (F/O) ratios of 0.5, 1.5, 2, and 2.5, and the produced products were named U0.5, U1.5, U2, and U2.5, respectively. The afore-mentioned combustion experiment was similarly repeated by employing different quantities of L-alanine and glycine fuels in such a way that Φ_c = (F/O) = 0.5, 1, 1.5, 2, and 2.5. The products were calcined at 500 °C for 1 h, and they were referred to as A0.5, A1, A1.5, A2, and A2.5 (for L-alanine fuel) and G0.5, G1, G1.5, G2, and G2.5 (for glycine fuel), respectively. Scheme 1 outlines the applied combustion processes.

2.3. Materials characterization

The phase purity and structure of the as-synthesized products were characterized using powder X-ray diffraction (XRD)

Scheme 1 Schematic representation of the combustion process.

patterns collected by 18 kW diffractometer (Bruker; model D8 Advance) with monochromated Cu-Kα radiation ($\lambda = 1.54178$ Å). Morphology of the as-prepared materials was identified employing a field emission scanning electron microscope (FE-SEM) connected with a microscope (FE-SEM) (JEOL JSM-6500F) and a high-resolution transmission electron microscope (HR-TEM) (JEM-2100) at 200 kV accelerating voltage. FT-IR spectra of the products in the range of 4000–400 cm^{-1} were measured on FT-IR spectrometer (Thermo Scientific; model Nicolet iS10) using KBr pellets. Thermal properties of the as-prepared materials were studied using simultaneous thermogravimetric (TGA)/differential thermal analyzer (DTA) (Shimadzu; model TA-60WS, Japan). The samples were thermally studied under an atmosphere of nitrogen gas with 20 °C min heating rate. Platinum crucible and alumina powder reference were used for the measurements of the phase changes and weight losses of the sample, respectively. The UV-vis spectra were recorded on a UV-visible spectrophotometer (Jasco, model v670).

2.4. Adsorption studies

The adsorption properties of the as-synthesized TiO$_2$ products were investigated by performing batch experiments in dark – to avoid the photocatalytic effect – using Reactive Red 195 dye (RR195) as a textile dye pollutant. The adsorption investigation was carried out using nano-sized TiO$_2$ products generated from the combustion reaction using urea fuel at an equivalence ratio, Φ_c, of 1. In a typical batch adsorption experiment: 0.05 g of TiO$_2$ nano-adsorbent was suspended in 25 mL of RR195 dye solution using a specific initial concentration ($C_0 = 100$ mg L^{-1}) at 25 °C temperature, pH 2, and 400 rpm stirring speed. Notably, pH of the dye solution was first adjusted using HCl and/or NaOH aqueous solutions (0.2 M) then TiO$_2$ nanoparticles were added. The suspension was allowed to magnetically stir; then, at fixed contact time intervals, aliquots of the adsorption media were withdrawn and centrifuged to separate the TiO$_2$ nano-adsorbent. We determined the residual dye concentration in the separated supernatant employing a pre-constructed calibration curve on a UV-vis spectrophotometer for RR195 dye at $\lambda_{max} = 542$ nm. We determined the adsorption capacity (q_t, mg g^{-1}) of TiO$_2$ adsorbent utilizing eqn (1). We also estimated the dye percent removal efficiency (% R) using eqn (2).

$$q_t = \frac{V(C_0 - C_t)}{m} \tag{1}$$

$$\%\ R = \frac{(C_0 - C_t)}{C_0} \times 100 \tag{2}$$

where, C_0 (mg L^{-1}) and C_t (mg L^{-1}) are the initial dye concentration and concentration of the dye solution at time t of the adsorption process, respectively. Besides, V (L) and m (g) are the dye solution volume and mass of the TiO$_2$ nano-adsorbent, respectively. Moreover, we have studied the different parameters influencing the adsorption process such as pH (1–10), contact time (5–240 min), initial dye concentration (50–500 mg L^{-1}), temperature (298–318 K), and KCl dose (0.05–0.45 g). We

estimated the equilibrium adsorption capacity (q_e, mg g^{-1}) of the TiO$_2$ nano-adsorbent using eqn (3).

$$q_e = \frac{V(C_0 - C_e)}{m} \tag{3}$$

where, C_e (mg L^{-1}) is the equilibrium dye concentration (i.e. the remaining dye concentration in the supernatant at equilibrium). The other terms of eqn (3) have the previously mentioned meaning.
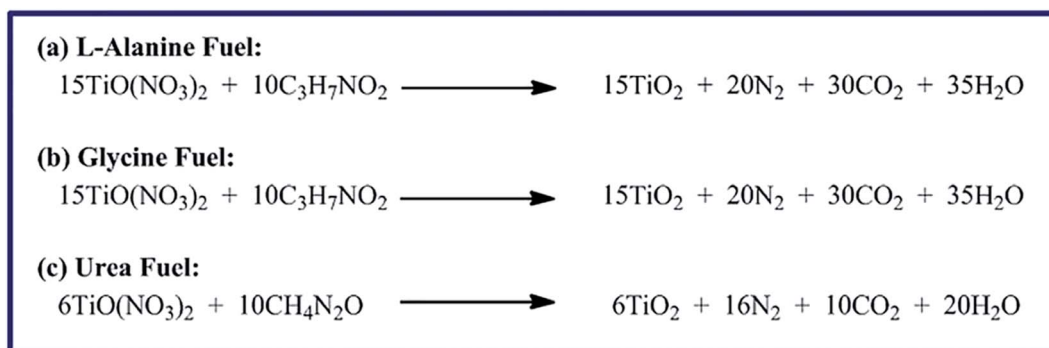
3.   Results and discussion

3.1. Auto-combustion synthesis and characterization of TiO$_2$ nanoparticles

In our earlier investigation, we have prepared MgAl$_2$O$_4$ and MgO nanostructures via a combustion method using metal nitrate salts and various fuels.[8] We found that the fuel type has a significant influence on the crystallite size of MgAl$_2$O$_4$ and MgO products, but we used only one equivalence ratio (Φ_c) value. Therefore, in this vein, we have extensively investigated the effect of fuel type and equivalence ratio (Φ_c) on the combustion of titanyl nitrate (oxidant). The study revealed that the type and quantity of the fuel have a remarkable impact on the product composition, crystal size, and morphology, as it will be shortly discussed. Hence, TiCl$_4$ as a relatively inexpensive material was converted into TiO(NO$_3$)$_2$.[37,38] The combustion reactions were performed using the in situ generated TiO(NO$_3$)$_2$ as an oxidizer and L-alanine, glycine, and urea as fuels, separately. Moreover, different fuel-to-oxidant equivalence ratios (Φ_c): 0.5, 1, 1.5, 2, and 2.5, have been examined to produce the most appropriate TiO$_2$ nanoparticles for the removal of RR195 textile dye from aqueous media. The combustion reactions of TiO(NO$_3$)$_2$ and different fuels: L-alanine, glycine, and urea, separately, at $\Phi_c = 1$, as a representative example, can be proposed as given in Scheme 2. The ignited and calcined products were identified by means of XRD, SEM, TEM, FR-IR, TGA/DTA, and BET analyses.

3.1.1. XRD investigation. The crystallinity and phase compositions of the combustion synthesized products were identified employing the X-ray diffraction technique. Fig. S1 (ESI†), S2 (ESI†) and (1) exhibit the XRD patterns of the calcined products: (A0.5–A2.5), (G0.5–G2.5), and (U0.5–U2.5), prepared via a combustion process using L-alanine, glycine, and urea fuels, respectively. Inspection of these XRD figures revealed that the fuel and its quantity have a significant influence on the phase composition and crystallinity of the products. Using L-alanine fuel in the combustion process produced pure tetragonal anatase TiO$_2$ product (JCPDS file no. 01-084-1286) at $\Phi_c = 0.5$ (Fig. S1(a), ESI†), while other Φ_c values produced tetragonal anatase (JCPDS file no. 01-084-1286) and orthorhombic brookite TiO$_2$ (JCPDS file no. 01-076-1937) phases. It is also observed that the brookite phase became more predominant as the Φ_c value increased (i.e. $\Phi_c > 0.5$), as shown in Fig. S1(b–e), ESI† The average crystallite sizes of the calcined products were determined using the Debye–Scherrer equation (eqn (4)) and tabulated in Table (1).[39]

$$D = 0.9\lambda/\beta \cos\theta_B \tag{4}$$

(a) L-Alanine Fuel:

$$15TiO(NO_3)_2 + 10C_3H_7NO_2 \longrightarrow 15TiO_2 + 20N_2 + 30CO_2 + 35H_2O$$

(b) Glycine Fuel:

$$15TiO(NO_3)_2 + 10C_3H_7NO_2 \longrightarrow 15TiO_2 + 20N_2 + 30CO_2 + 35H_2O$$

(c) Urea Fuel:

$$6TiO(NO_3)_2 + 10CH_4N_2O \longrightarrow 6TiO_2 + 16N_2 + 10CO_2 + 20H_2O$$

Scheme 2 The proposed combustion reactions of titanyl nitrate with L-alanine, glycine, and urea fuels.

where, λ, β, and θ_B symbols are wavelength of the X-ray radiation (nm), the diffraction peak full width at half maximum (FWHM), and angle of the Bragg diffraction, respectively.

However, combustion reactions of $TiO(NO_3)_2$ and glycine fuel gave pure tetragonal anatase TiO_2 phase at all used fuel-to-oxidant relative equivalence ratio (Φ_c) values: 0.5, 1.0, 1.5, 2.0, and 2.5. And all the XRD patterns of the products (G0.5–G2.5, Fig. S2, ESI†) could be indexed well to diffraction peaks of pure tetragonal anatase TiO_2 with cell constants: $a = 3.782$ Å, $b = 3.782$ Å, and $c = 9.502$ Å (space group $I4_1/amd$, JCPDS card 01-084-1286). No other diffraction peaks for other TiO_2 phases could be observed. These data are consistent with the reported ones.[34] Moreover, the average crystallite size of the calcined products was calculated using eqn (4) and listed in Table 1. The results showed that increasing the Φ_c values from 0.5 to 2.5 (i.e. increasing the quantity of the glycine fuel) resulted in increasing the crystallite size of the calcined products from 13.0 to 24.9 nm, respectively. This can probably be returned to that increasing the amount of the used glycine fuel in the combustion process may increase the quantity of heat generating from

this process. Consequently, this may result in increasing the temperature during the TiO_2 particles crystal growth.

On the other hand, employing urea as fuel in the combustion of $TiO(NO_3)_2$, produced single tetragonal anatase TiO_2 phase (space group $I4_1/amd$, JCPDS card 01-084-1286) at Φ_c values of 0.5 and 1.0 (Fig. 1). The average crystallite sizes of the corresponding calcined products were 11.6 and 11.9 nm, respectively, as presented in Table 1. No other reflections for other TiO_2 phases have been detected. Additionally, at higher Φ_c values ($\Phi_c > 1.0$), the combustion reaction gave a mixture of anatase (JCPDS card 01-084-1286) and rutile (JCPDS card 01-087-0920) TiO_2 phases, as depicted in Fig. 1. Besides, the value of the rutile to anatase phase ratio increased from 46.7 : 53.3 to 89.4 : 10.6 with increasing the Φ_c values from 1.5 to 2.5, respectively, as shown in Table 1. The average crystallite size was enhanced also with increasing the Φ_c values (i.e. the quantity of urea fuel). These results can be attributed to that higher values of Φ_c may result in a higher quantity of heat which can raise the temperature of the system, and this high temperature can consequently convert the anatase phase into the rutile phase.[40] These higher temperatures can also

Table 1 The produced phases, crystallite sizes, and corresponding maximum adsorption capacities of the TiO_2 products as well as the used fuels in the combustion processes

Fuel	Equivalence ratio, Φ_c	Product phases[a]	Sample label	Crystallite size, nm	Maximum adsorption capacity, q_m (mg g^{-1})
L-Alanine	0.5	A	A0.5	13.0	77.00
	1.0	A + B	A1	15.8	42.00
	1.5	A + B	A1.5	16.0	40.00
	2.0	A + B	A2	22.0	36.90
	2.5	A + B	A2.5	23.3	35.00
Glycine	0.5	A	G0.5	13.0	52.00
	1.0	A	G1	18.0	87.00
	1.5	A	G1.5	20.0	65.00
	2.0	A	G2	23.0	62.40
	2.5	A	G2.5	24.9	62.00
Urea	0.5	A	U0.5	11.6	132.0
	1.0	A	U1	11.9	126.0
	1.5	A + R	U1.5	21.0	65.00
	2.0	A + R	U2	30.7	51.50
	2.5	A + R	U2.5	68.0	39.50

[a] Where, A, B, and R stand for anatase, rutile, and Brookite phases of the TiO_2 products, respectively, and the adsorption conditions were 300 mg L^{-1} initial dye concentration, pH 2, temperature 25 °C, and 0.05 g adsorbent dose for this adsorption study.
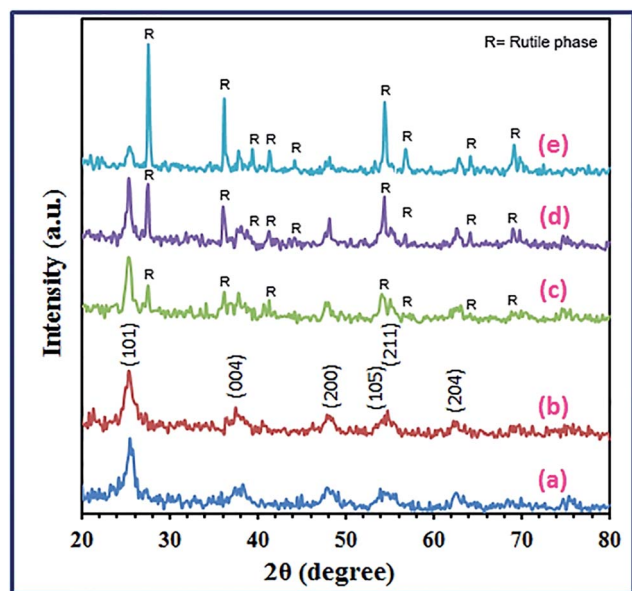
Fig. 1 XRD patterns of the as-synthesized TiO_2 products calcined at 500 °C using urea fuel.

Fig. 2 FT-IR spectra of the as-synthesized TiO_2 products before calcination: (a), (b), and (c), for L-alanine, glycine, and urea fuels, respectively, after calcination at 500 °C for the corresponding products (d–f), respectively, and RR195 dye loaded TiO_2 nano-adsorbent (g).

enhance the crystallinity of the TiO_2 products.[40] In addition, the XRD patterns (Fig. 1) have not revealed any peaks for brookite phase in the products: U0.5–U2.5. Thus, the fuel type and fuel-to-oxidant relative equivalence ratio value (Φ_c) can significantly control both the crystallite size and/or phase of the nanosized TiO_2 products, through the combustion route. Moreover, urea fuel can be chosen as the optimum fuel in our study since it generates pure anatase phase with the smallest crystallite size which is appropriate for the present adsorption studies.

3.1.2. FT-IR investigation. The chemical structures of the combustion products were investigated using the FT-IR spectra. Fig. 2 exhibits the FT-IR spectra of the combustion products prepared using L-alanine, glycine, and urea fuels at fuel-to-oxidant relative equivalence ratio value of 1.0 (*i.e.* $\Phi_c = 1.0$). We focused on the combustion products, before and after calcination, at $\Phi_c = 1.0$ because this value generated TiO_2 products with almost the smallest crystallite size and the most appropriate adsorption properties. The FT-IR spectra of the samples before calcination, Fig. 2(a–c), showed vibrational absorptions at 2900 and 1360 cm^{-1} which might be attributed to the organic content residues.[41] Besides, more peaks appeared in the range of 1490–1016 cm^{-1} for the combustion product of the glycine fuel (Fig. 2(b)), and this might be due to Ti–O–C and organic content residue.[41,42] All the FT-IR spectra of the combustion products before calcination (Fig. 2(a–c)) showed vibrational absorptions in the range of 410–600 cm^{-1} corresponding to Ti–O–Ti bond.[42,43] Additionally, two absorption peaks appeared at *ca.* 1590 and 3370 cm^{-1} may be attributed to the bending and stretching vibrations of the adsorbed water molecules.[44–47] However, on calcination of the combustion products, Fig. 2(d–f), the vibrational peaks due to the organic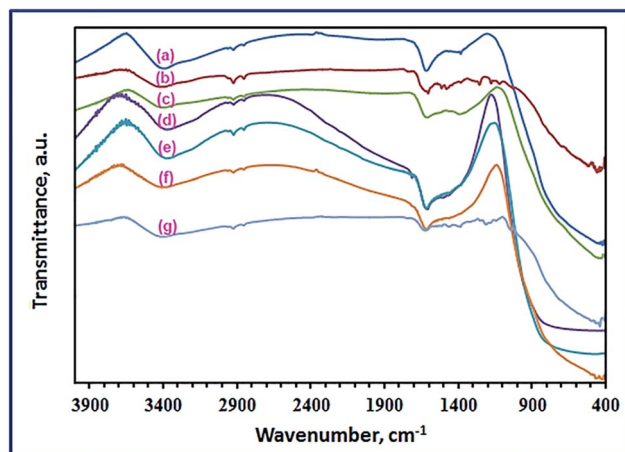 residues disappeared. The FT-IR spectra of the calcined products showed one peak at *ca.* 410–600 cm^{-1} attributing to Ti–O–Ti bond.[42,43] The spectra showed also two vibrational peaks at *ca.* 1590 and 3370 cm^{-1} due to bending and stretching vibrations, respectively, of the adsorbed water molecules.

3.1.3. Morphological investigation. Morphology of the as-synthesized TiO_2 nanoparticles calcined at 500 °C (A1, G1, and U1) was studied employing field-emission scanning electron microscope (FE-SEM) and transmission electron microscope (TEM), as displayed in Fig. (3) and (4), respectively. The low and high magnification FE-SEM images of the TiO_2 product (A1) generated from L-alanine fuel and presented in Fig. 3(a) and (b), respectively, indicate that the TiO_2 product is composed of spherical particles with 1.5 μm diameter. Besides, glycine fuel generated TiO_2 product (G1) with irregular flake shapes as shown from its low and high magnification FE-SEM images (Fig. 3(c) and (d)). On the other hand, urea fuel produced TiO_2 product (U1) with aggregates of hexagonal, pyramidal, and irregular shapes as shown in low magnification FE-SEM image (Fig. 3(e)). However, high magnification FE-SEM image (Fig. 3(f)) of the product reveals that the aggregates are composed of nanosphere-like particles with an average diameter of *ca.* 90 nm. Consequently, utilizing different fuels at varying fuel-to-oxidant relative equivalence ratios in the combustion process might produce different quantities of heat and gasses during the combustion process which resulted in TiO_2 products with different morphological structures. And this also gave TiO_2 products with different crystallite sizes. These results are consistent with the reported data.[34] Besides, microstructural investigation of the TiO_2 products using transmission electron microscopy (TEM), Fig. 4(a–c), indicated that the three fuels produced similar morphologies for the TiO_2 particles which were hexagon, sphere, and cube-like structures. The TEM images also revealed the porous structures of the products. The average particle size of the generated TiO_2 products: A1, G1, and
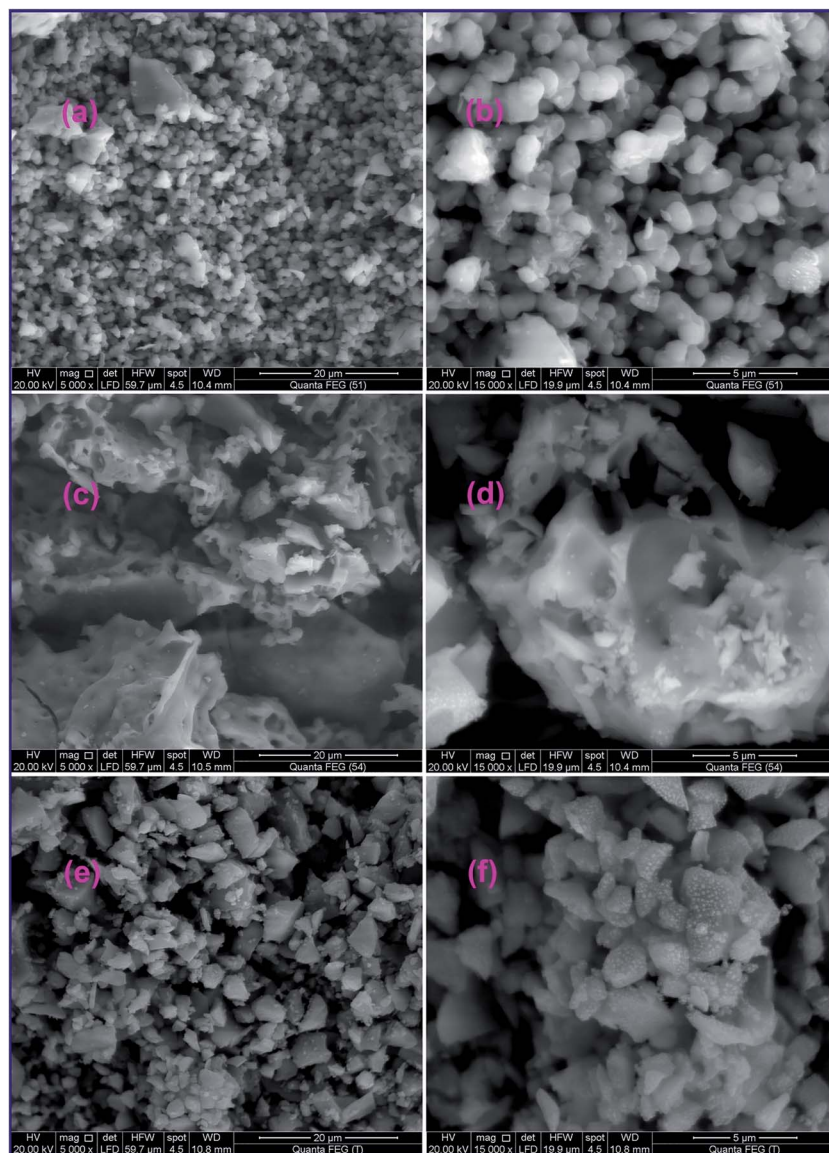
Fig. 3 FE–SEM images of the as-synthesized TiO₂ products calcined at 500 °C, using L-alanine (a and b), glycine (c and d), and urea (e and f) fuels.

U1, was 17, 20, and 12 nm, respectively, which was consistent with the results calculated from the XRD data.

3.1.4. Thermal investigation. Thermal analyses (TG/DTA) of the combustion products generated from the fuels under study at $\Phi_c = 1.0$, before calcination, are presented in Fig. 5(a–c). Fig. 5(a(i)) displays the TG curve of the combustion product before calcination while L-alanine is used as fuel. This figure reveals two mass loss steps. The first degradation step (mass loss of 7.562%) may be attributed to the removal of physically adsorbed water molecules, and it is detected in the temperature range of 48–300 °C. The second decomposition step (mass loss of 3.074%) observed in the range of 300–650 °C might correspond to decomposition of the remaining L-alanine fuel and carbon residues left from the combustion process. The TG curve (Fig. 5(b(i))) of the combustion product, in the case of glycine fuel, revealed two mass losses. The first one (mass loss of 5.185%) was broad, and it might be due to the elimination of

the adsorbed water molecules appeared in the temperature range of 48–225 °C. The second step (mass loss of 7.557%) was also broad, and it might be two overlapped decomposition steps. It was observed in the temperature range of 225–650 °C, and it might be due to the decomposition of the remaining glycine and carbon residues. Thermal decomposition of the combustion product in case of urea fuel revealed two decomposition steps (Fig. 5(c(i))). The first one (mass loss of 5.055%) was detected in the temperature range of 48–175 °C due to the removal of the adsorbed water molecules. The second one (mass loss of 7.013%) was observed in the temperature range of 175–500 °C. This second stage was broad, and it might be two overlapped steps merged together due to the decomposition of the remaining urea fuel and carbon residues generated from the combustion process. The DTA analyses confirmed the results collected from the TG curves. DTA curve, Fig. 5(a(ii)), of the combustion product from the L-alanine fuel showed one
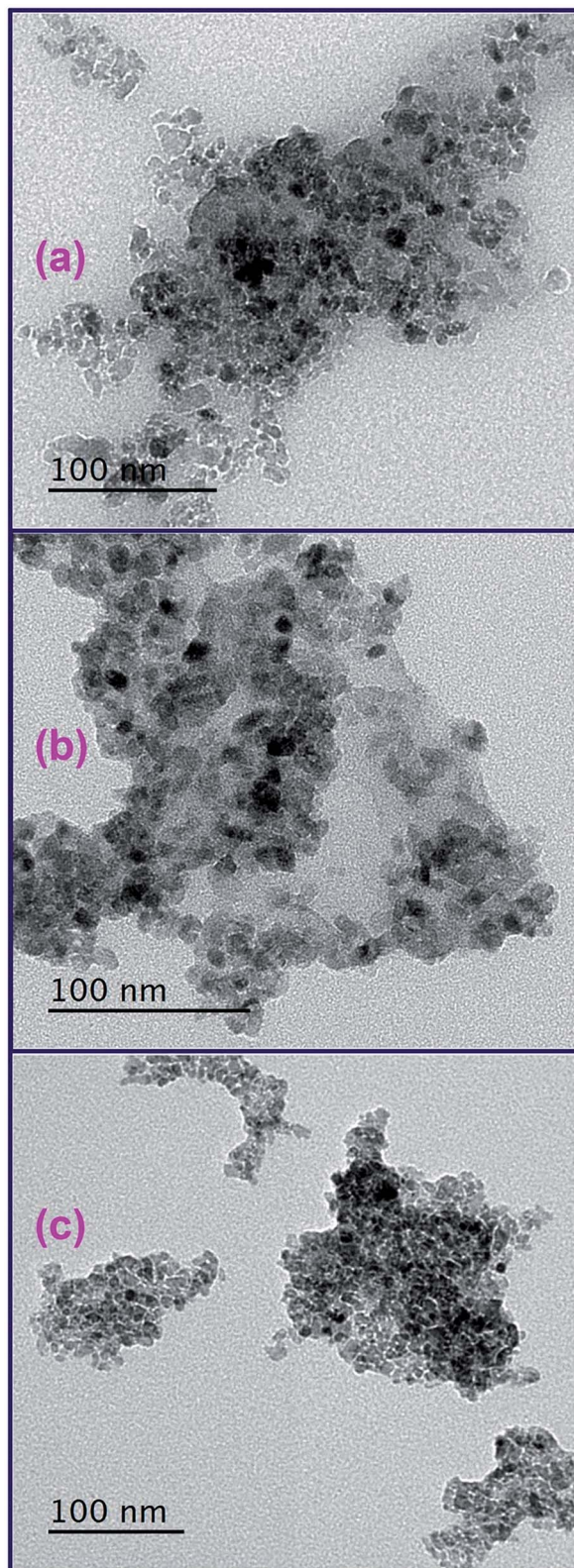
Fig. 4   TEM images of the as-synthesized TiO_2 products calcined at 500 °C, using L-alanine (a), glycine (b), and urea (c) fuels.

endothermic peak at *ca.* 76.72 °C corresponding the elimination of the adsorbed water. This figure also exhibited one exothermic peak at *ca.* 451.9 °C attributing to the decomposition of the L-alanine and carbon residues. Fig. 5(b(ii)) shows the DTA curve of the combustion product in case of glycine fuel. This figure showed complex DTA curve with very broad peaks: endothermic one at *ca.* 77.00 °C, exothermic one at *ca.* 420.0 °C, and exothermic one at *ca.* 450.0 °C. These peaks can be attributed to the removal of adsorbed water molecules, decomposition of the remaining glycine residue, and decomposition of the carbon residue, respectively. Finally, Fig. 5(c(ii)) displays the DTA analysis of the combustion product when urea is used as a fuel. This figure reveals three peaks: endothermic peak at *ca.* 83.52 °C, exothermic peak at *ca.* 276.6 °C, and exothermic broad peak at *ca.* 350.0 °C. The first one can be due to the removal of the adsorbed water molecules, the second one may be assigned to the decomposition of some of the remaining urea residue, and the last peak can be attributed to the decomposition of the carbon residue left from the combustion process, respectively. It is noteworthy that decomposition of the residue fuel after the combustion process during the thermal analyses was also reported by others.[48]

3.1.5.   Textural structure and point of zero charge investigation. We investigated the texture properties of only the calcined TiO_2 product (U1) prepared using urea fuel at $\Phi_c = 1.0$ since this fuel gave TiO_2 product with almost the smallest crystallite size and the best adsorption properties. Besides, the combustion reactions presented in Scheme 1 reveal that urea fuel generates the largest quantity of gasses; consequently, because of these evolved gasses, TEM study, and the reported data, this fuel can produce the most porous TiO_2 product.[34] We carried out nitrogen gas adsorption–desorption isotherm measurement for the calcined TiO_2 product (U1) as depicted in Fig. S3(a), ESI.† Fig. S3(a)† reveals an adsorption–desorption isotherm with a hysteresis phenomenon. The isotherm is consistent with the type-IV isotherm for the mesoporous materials (*i.e.* 2–50 nm in size) based on the International Union of Pure and Applied Chemistry IUPAC classification.[49] The obtained Barret–Joyner–Halenda (BJH) pore volume and BET surface area for TiO_2 product (U1) were found to be 0.180 $cm^3\ g^{-1}$ and 115.379 $m^2\ g^{-1}$, respectively. Besides, the study exhibited that most of the sample pore volume was occupied with 31.2 nm diameter pores. Moreover, the point of zero charge (pH_{PZC}) of the as-prepared TiO_2 product (U1) was estimated because the surface charge of the nanoparticles suspended in a medium is dependent on the pH values of that medium as reported previously.[38] The point of zero charge value (pH_{pzc}) of TiO_2 nanoparticles was determined using the reported pH drift method[2,4,50] where we used TiO_2 suspensions in sodium chloride solutions (0.01 M) of various initial pH values in the range of 1.3–11. Then the pH_{pzc} value is the intersection point between the $pH_{initial} - pH_{final}$ and $pH_{initial} = pH_{final}$ curves, as displayed in Fig. S3(b), ESI.† The pH_{pzc} value of the as-prepared TiO_2 nanoparticles (U1) was estimated to be around 7.6 which is in good agreement with reported value.[51] However, it is worthy to mention that the pH_{pzc} values of the nano-sized metal oxides can vary widely depending on several parameters including chemical and surface modification, crystallite size, and particle transformation.[52]
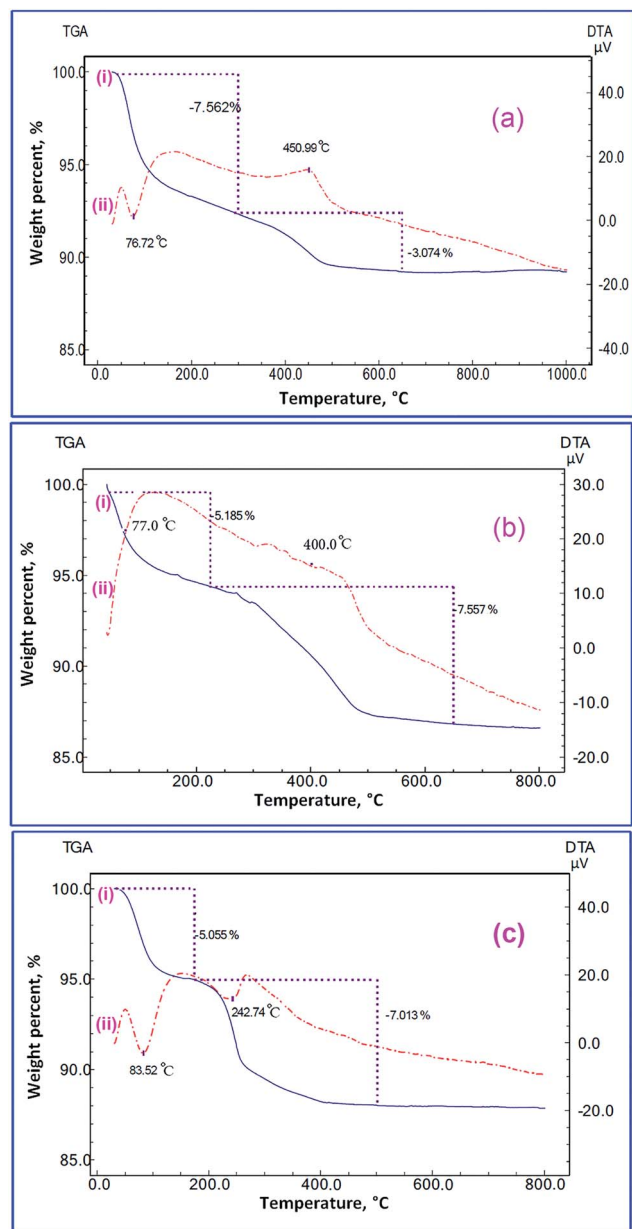
Fig. 5 TG (i), and DTA (ii) analyses of the TiO_2 combustion products; using L-alanine (a), glycine (b), and urea (c) fuels, under nitrogen gas.

3.2. Adsorption properties of the as-prepared TiO_2 nano-adsorbent

We investigated the adsorption properties of the TiO_2 product (U1) using Reactive Red 195 (RR195) dye as a pollutant and textile dye model. As explained by Nassar *et al.* the FT-IR spectra can be utilized as an evidence for the adsorption of dyes on adsorbents.[2,3,20] Fig. 2(f and g) depicts the FT-IR spectra of the TiO_2 adsorbent (U1) before and after RR195 dye adsorption, respectively. It is observed that the FT-IR spectrum of the RR195 dye-loaded TiO_2 differs from that of the bare TiO_2 before adsorption. The vibrational absorptions appeared at *ca.* 424, 3364 cm^{-1} of the pure TiO_2 nano-adsorbent (Fig. 2(f)) have been shifted to *ca.* 406 and 3374 cm^{-1}, respectively, after the

adsorption process. Besides, some new absorption peaks appeared upon RR195 dye adsorption at *ca.* 1004, 1174, 1364, and 1418 cm^{-1} as shown in the FT-IR spectrum of the RR195-loaded TiO_2 (Fig. 2(f)). These new peaks are probably due to the adsorbed RR195 dye molecules onto TiO_2 nano-adsorbent. Moreover, several parameters influencing the adsorption properties of the as-prepared nano-adsorbent (TiO_2) such as pH, contact time, initial dye concentration, ionic strength, and temperature have been investigated. Moreover, the effect of the used fuel – during the combustion process – on the adsorption capacities of the TiO_2 products (A0.5–U2.5) has also been studied as it will be shortly discussed.

3.2.1. Influence of pH. Adsorption media pH is one of the crucial parameters controlling the adsorption efficiency of dye molecules onto adsorbent nanoparticles. This parameter was studied under adsorption conditions: initial pH (1–10), initial dye concentration ($C_0 = 100$ mg L^{-1}), a TiO_2 adsorbent dose of 0.05 g, stirring rate of 400 rpm, a temperature of 25 °C, and contact time of 24 h. The results are displayed in Fig. 6(a). The data revealed that the adsorption of RR195 dye was pH dependent, and the maximum adsorption was observed in the pH range of 1–3. Afterward, the dye removal percent decreased slowly by increasing pH up to *ca.* 6 then it decreased significantly at higher pH values. Therefore, the optimum pH value of the adsorption process of interest was chosen as pH 2; consequently, the other adsorption experiments were performed at pH 2. Moreover, the effect of solution pH on the adsorption of RR195 dye on TiO_2 nano-adsorbent could be explained by taking into our account the surface charges of both the TiO_2 particles and RR195 dye molecules. Because pH_{pzc} of the as-prepared TiO_2 product was estimated to be 7.6, the surface of TiO_2 nanoparticles, (MOH), would be positively charged due to their covering with H^+ ions (MOH_2^+). Besides, the anionic dye molecules behave as anionic species (*i.e.* negatively charged species) causing high electrostatic attraction which results in higher adsorption. While at higher pH values, OH^- anions will interact with the TiO_2 (MOH) forming deprotonated oxide particles (MO^-); consequently, there will be repulsion forces between the similar negatively species (*i.e.* dye molecules and TiO_2 particles). Besides, at higher pH values there will be a competition between the negatively charged dye molecules and OH^- anions during the adsorption process. These result in a decrease in the adsorption of the dye molecules at higher pH values. Therefore, the acidic medium is more favorable for the adsorption of RR195 dye on TiO_2 nano-adsorbent, and the electrostatic interaction may be the most predominant adsorption mechanism.[53] Similar results have been reported in the literature for the adsorption of some dyes.[53,54]

3.2.2. Contact time and adsorption kinetic investigation. The effect of contact time of the adsorption of RR195 dye on the as-prepared TiO_2 nano-adsorbent was investigated under the adsorption conditions: initial dye concentrations (50–250 mg L^{-1}), pH 2, temperature of 25 °C, and 0.05 g adsorbent dose. The adsorption capacities (q_t, mg g^{-1}) of TiO_2 nano-adsorbent for the adsorption of RR195 dye *versus* the contact time (t, min) were displayed in Fig. 7(a) for various initial dye concentrations. It could be observed that the adsorption was fast in the initial
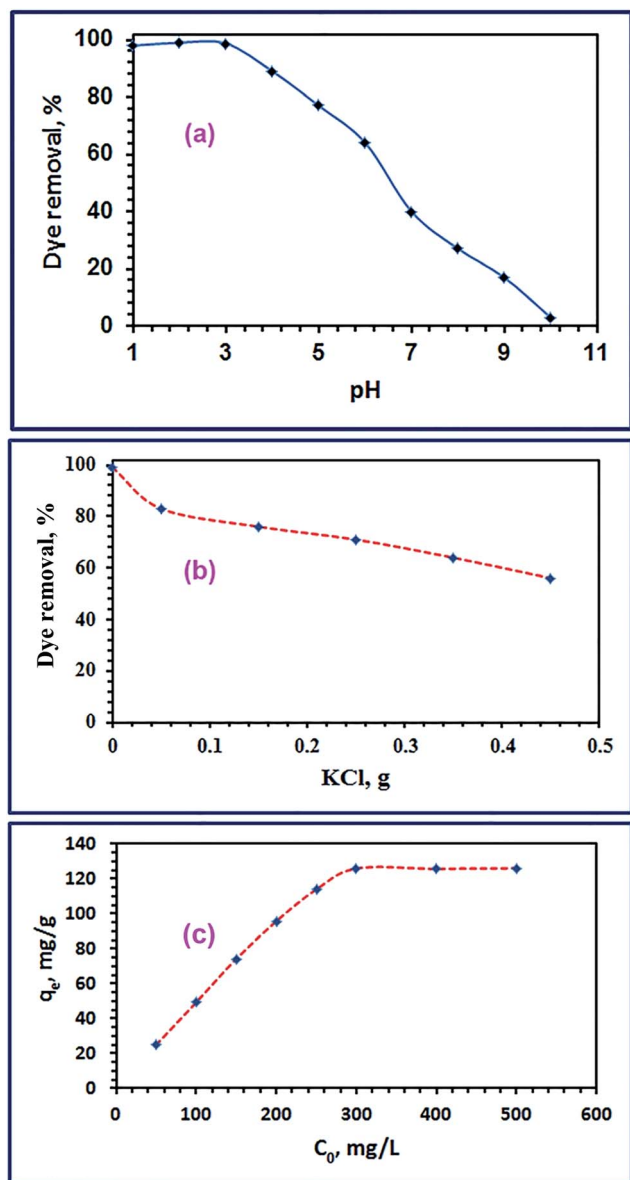
Fig. 6 Effect of pH (a), KCl concentration (b), and initial RR195 dye concentration (c) on adsorption of RR195 dye on TiO$_2$ nano-adsorbent (b).
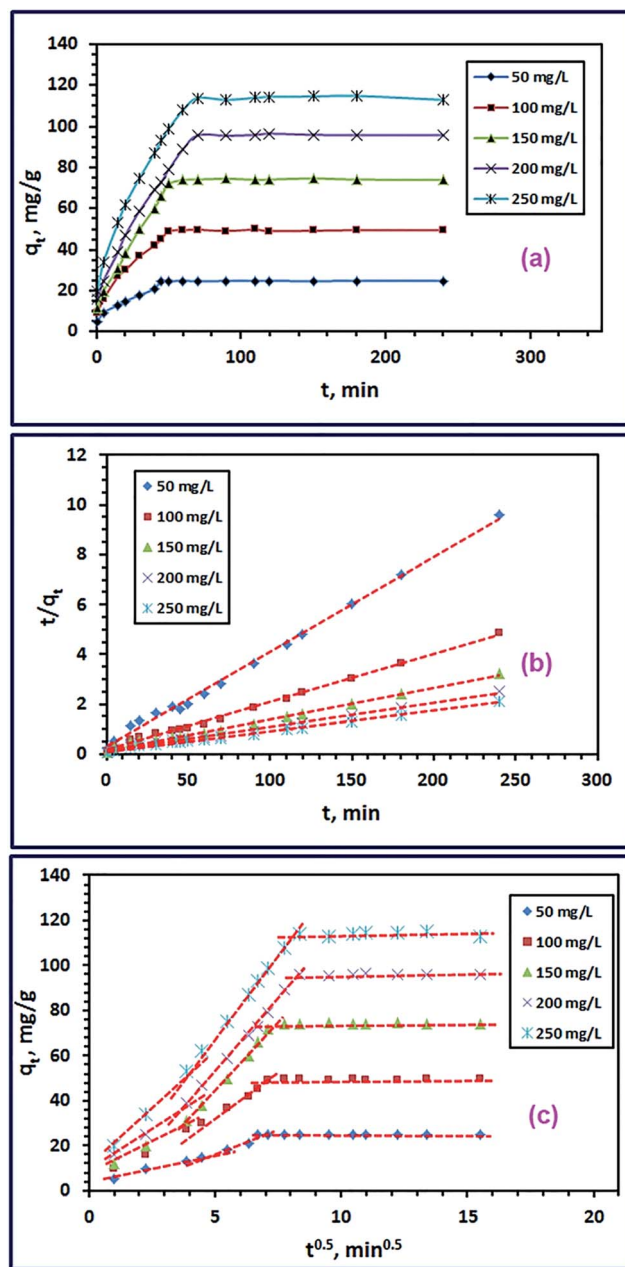

Fig. 7 Effect of contact time at various initial dye concentrations (a), pseudo-second-order (b) and intra-particle diffusion model (c) for the RR195 dye adsorption on TiO$_2$ nano-adsorbent.

stages; afterward, it increased slowly with increasing the contact time until it reached the equilibrium state (*i.e.* the plateau behavior). The change in the rate of RR195 dye adsorption at the initial and later stages is probably due to the presence of larger number of active adsorption sites available for adsorption in the beginning of the adsorption process. Then, this number decreased with increasing the contact time by an occupation of the adsorption active sites during the adsorption process. Besides, the slower adsorption rates at longer contact times can be assigned to the slower pore diffusion rate of the RR195 dye molecules into the TiO$_2$ nanoparticles. This behavior is similar to that reported for the adsorption of RB5 dye on ZnO nano-particles.[4] In order to understand the adsorption mechanism, the experimental kinetic data of RR195 dye adsorption on TiO$_2$

adsorbent were examined using pseudo-first-order[55] and pseudo-second-order[56] models expressed by eqn (5) and (6), respectively.

$$\log(q_e - q_t) = \log q_e - \frac{k_1}{2.303} t \qquad (5)$$

$$\frac{t}{q_t} = \frac{1}{k_2 \, q_e{}^2} + \frac{t}{q_e} \qquad (6)$$

where, q_t (mg g^{-1}) and q_e (mg g^{-1}) are the adsorption capacity and equilibrium adsorption capacity of TiO$_2$ adsorbent at time t (min) and equilibrium time, respectively. k_1 (min^{-1}) and k_2 (g mg^{-1} min^{-1}) are the rate constant of pseudo-first-order

adsorption process and pseudo-second-order adsorption process, respectively. Linear plot of $\log(q_e - q_t)$ against t (eqn (5)) was performed for various initial dye concentrations to calculate the $q_{e(cal)}$ and k_1 constants for pseudo-first-order model (not shown here). Besides, $q_{e(cal)}$ and k_2 constants of the pseudo-second-order model were estimated *via* plotting of t/q_t against t (eqn (6)) for various initial dye concentrations, as presented in Fig. 7(b). The calculated kinetic constants for different initial dye concentrations are tabulated in Table 2. Comparison between regression coefficient (r^2) values indicates that the pseudo-second-order model is more valid than the pseudo-first-order model for two reasons. The first one is that the r^2 values of the pseudo-second-order model is closer to unity than those of the pseudo-first-order model. The second reason is that the adsorption capacity ($q_{e(cal)}$) values calculated from the pseudo-second-order model is closer to the experimentally obtained ones compared to those estimated from the pseudo-first-order model. Moreover, using the calculated pseudo-second-order rate constants and adsorption capacities ($q_{e(cal)}$), the initial sorption rate (h) can be determined using eqn (7) and listed in Table 2.[57] The tabulated initial sorption rate values indicated that they increased with enhancing the initial dye concentrations.

$$h = k_2 q_e^2 \qquad (7)$$

To investigate the influence of the intra-particle diffusion resistance on the adsorption, the intra-particle diffusion model (eqn (8)) was applied.[58]

$$q_t = k_i t^{0.5} + C \qquad (8)$$

where, q_t (mg g^{-1}), t (min), C (mg g^{-1}), and k_i (mg (g min$^{1/2}$)$^{-1}$) are the quantity of the adsorbed RR195 dye at time t (min), the intercept indicating the boundary layer thickness, and intra-particle diffusion rate constant. Fig. 7(c) shows the plot of q_t against $t^{0.5}$ values, and the corresponding constants are listed in Table 2. Fig. 7(c) revealed that the obtained curves were multi-linear plots, and they did not pass the origin. Consequently, the rate-determining step of this adsorption process is not only controlled by the intra-particle diffusion mechanism but also controlled by other mechanisms including film diffusion and bulk diffusion.[59]

3.2.3. Influence of ionic strength.
Industrial effluents often contain various inorganic salts including KCl, and others, as well as the organic pollutants. These inorganic salts can compete with organic dye molecules for the active adsorption sites of adsorbents during the adsorption process; consequently, this may decrease the adsorption efficiency of the adsorbents. The influence of these competing inorganic ions raises an essential issue since they can control both the electrostatic and non-electrostatic interactions which may be held between the adsorbate and the adsorbent surface.[38] We investigated the effect of KCl concentrations on the adsorption of RR195 dye using the as-prepared TiO$_2$ product as an adsorbent under the adsorption conditions: 100 mg L^{-1} initial dye concentrations, pH 2, temperature of 25 °C, and 0.05 g adsorbent dose. The experimental results depicted in Fig. 6(b) indicate that the dye removal efficiency decreases with increasing the potassium chloride concentration. This is consistent with the conclusion that the adsorption mechanism is mainly based on the electrostatic interactions between the dye molecules and charged surface TiO$_2$ particles.[17,38]

3.2.4. Initial concentration and adsorption isotherm investigation.
The effect of initial dye concentration on the adsorption process was examined using batch techniques under adsorption conditions: 0.05 g TiO$_2$, pH 2, initial dye concentrations (50.0–500 mg L^{-1}), *ca.* 70 min equilibration time, and at 25 °C temperature. The results are presented in Fig. 6(c). The results indicated that the adsorption capacity of TiO$_2$ adsorbent increased with increasing the initial dye concentration untill it reached the plateau with a maximum value ($q_{m(exp)}$) of 126.0 mg g^{-1}. It is noteworthy that increasing the adsorbed quantity of the RR195 dye with increasing its initial concentration is probably attributed to overcoming the resistance of the dye molecule mass transfer between the solid and liquid phases at higher dye concentrations during the adsorption process.[38,60] Besides, the plateau behavior might be due to the saturation of the limited number of the adsorption sites at high initial concentrations.[61]

Additionally, the experimentally obtained adsorption results were examined using the Langmuir and Freundlich adsorption isotherm models presented in eqn (9) and (10), respectively.

$$\frac{C_e}{q_e} = \frac{1}{K_L q_m} + \frac{C_e}{q_m} \qquad (9)$$

$$\ln q_e = \ln K_F + \frac{1}{n} \ln C_e \qquad (10)$$

Table 2 Parameters of the pseudo-second order model for the adsorption of RR195 dye on TiO$_2$ adsorbent at various initial dye concentrations (C_0)

Pseudo-second-order model					
C_0 (mg g^{-1})	K_2 [g (mg min)$^{-1}$]	$q_{e(cal)}$ (mg g^{-1})	r_1^2	H [g (mg min)$^{-1}$]	$q_{e(exp)}$ (mg g^{-1})
50	4.90×10^{-3}	26.23	0.996	3.369	24.90
100	2.37×10^{-3}	52.02	0.997	6.402	49.40
150	1.05×10^{-3}	79.92	0.992	6.717	74.30
200	0.590×10^{-3}	105.3	0.991	6.720	95.80
250	0.654×10^{-3}	122.6	0.994	9.832	114.0

where, C_e, q_e, q_m, and K_L are the dye equilibrium concentration (mg L^{-1}), equilibrium adsorption capacity (mg g^{-1}), maximum adsorption capacity (mg g^{-1}), and Langmuir constant (L mg^{-1}), respectively. Besides, K_F and n are the Freundlich constant which indicates the adsorption capacity and a constant indicating the adsorption intensity, respectively. The two isotherm models were checked by plotting C_e/q_e against C_e (eqn (9), Fig. 8(a)), and ln q_e versus ln C_e (eqn (10), Fig. 8(b)). The corresponding constants for each model were estimated from the slope and intercept of the relevant straight line, and they were tabulated in Table 3. The maximum adsorption capacity ($q_{m(cal)}$) of TiO$_2$ adsorbent calculated from the Langmuir model was found to be 127.0 mg g^{-1} which is compatible with the experimentally obtained one. On the other hand, $q_{m(cal)}$ was also determined based on the Freundlich isotherm model according to eqn (11) as reported by Halsey.[62]

$$K_F = \frac{q_m}{C_0^{1/n}} \qquad (11)$$

The maximum adsorption capacity ($q_{m(cal)}$) utilizing the Freundlich isotherm was estimated to be 167.34 mg g^{-1}. Comparison between the tabulated constants in Table (3) for both applied isotherm models exhibited that adsorption of RR195 dye on TiO$_2$ adsorbent followed the Langmuir adsorption isotherm. This is based on the following: (i) the regression coefficient value ($r^2 = 0.9999$) for the Langmuir isotherm model (Fig. 8(a)) higher than that of the Freundlich isotherm model (r^2

= 0.8348), and (ii) the maximum adsorption capacity ($q_{m(cal)}$) calculated from the Langmuir isotherm model is closer to the experimentally determined value than that obtained from the Freundlich isotherm model. Therefore, the obtained results indicate the TiO$_2$ homogenous nature and the RR195 dye monolayer coverage on the surface of the TiO$_2$ nano-adsorbent. In addition, the favorability of the adsorption of RR195 dye on the TiO$_2$ nano-adsorbent was examined using the separation factor constant (R_L) derived from the Langmuir isotherm model, as presented in eqn (12).

$$R_L = \frac{1}{1 + K_L C_0} \qquad (12)$$

where, C_0 and K_L are the initial dye concentration (mg L^{-1}) and Langmuir constant (L mg^{-1}), respectively. According to the literature, if $R_L = 0$, $0 < R_L < 1$, $R_L = 1$, or $R_L > 1$, the adsorption process will be irreversible, favorable, linear, or unfavorable, respectively.[63] The calculated R_L values for different initial dye concentrations were found to be less than one and greater than zero (0.0099–0.091) over the RR195 dye concentration range (50.0–500 mg L^{-1}), as listed in Table 3; consequently, the adsorption of RR195 dye on the as-prepared TiO$_2$ nano-adsorbent is favorable.

3.2.5. Adsorption thermodynamics. The effect of adsorption media temperatures on the adsorption of RR195 dye on the as-prepared TiO$_2$ product was explored in the range of 298–318 K under the adsorption conditions: 0.05 g TiO$_2$, 300 mg L^{-1} initial dye concentration, 400 rpm stirring rate, and ca. 2 h contact time. The results exhibited that the adsorption capacity of the as-prepared TiO$_2$ adsorbent enhances with increasing the temperature of the adsorption media meaning the endothermic nature of the adsorption process, as shown in Fig. 9(a). Furthermore, the thermodynamic constants can provide information on the energy changes associated with the adsorption process. Therefore, some thermodynamic parameters have been estimated including the enthalpy change (ΔH^0), entropy change (ΔS^0), and Gibbs free energy change (ΔG^0) through using eqn (13) and (14).[20]

$$\ln K_c = \frac{\Delta S^0}{R} - \frac{\Delta H^0}{RT} \qquad (13)$$

$$\Delta G^0 = \Delta H^0 - T\Delta S^0 \qquad (14)$$

where, R and T are the universal gas constant (8.314 × 10^{-3} kJ mol^{-1} K^{-1}) and adsorption medium absolute temperature (K), respectively. Moreover, K_c is the thermodynamic equilibrium constant and the value of this constant must be dimensionless. This is because the fact that the units of ΔG^0, R, and T in eqn (15) are kJ mol^{-1}, kJ mol^{-1} K^{-1}, and K, respectively. Therefore, some approaches have been proposed for the determination of a dimensionless thermodynamic equilibrium constant[64–69]
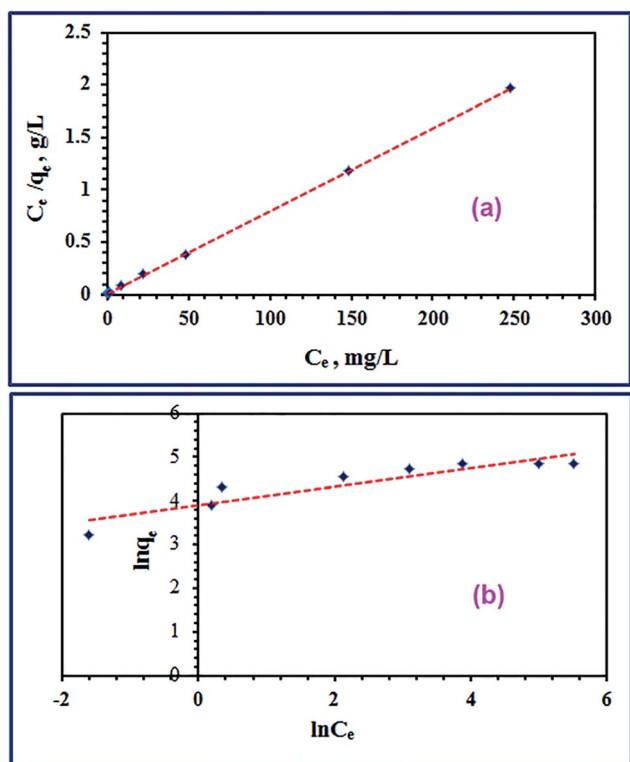
$$\Delta G^0 = RT \ln K_c \qquad (15)$$

Fig. 8 Langmuir (a) and Freundlich (b) isotherm models for the adsorption of RR195 dye on TiO$_2$ nano-adsorbent.

In our current study, we have calculated the dimensionless thermodynamic equilibrium constant (K_c) using two

Table 3 Langmuir and Freundlich isotherm constants for the adsorption of RR195 dye on TiO_2 adsorbent

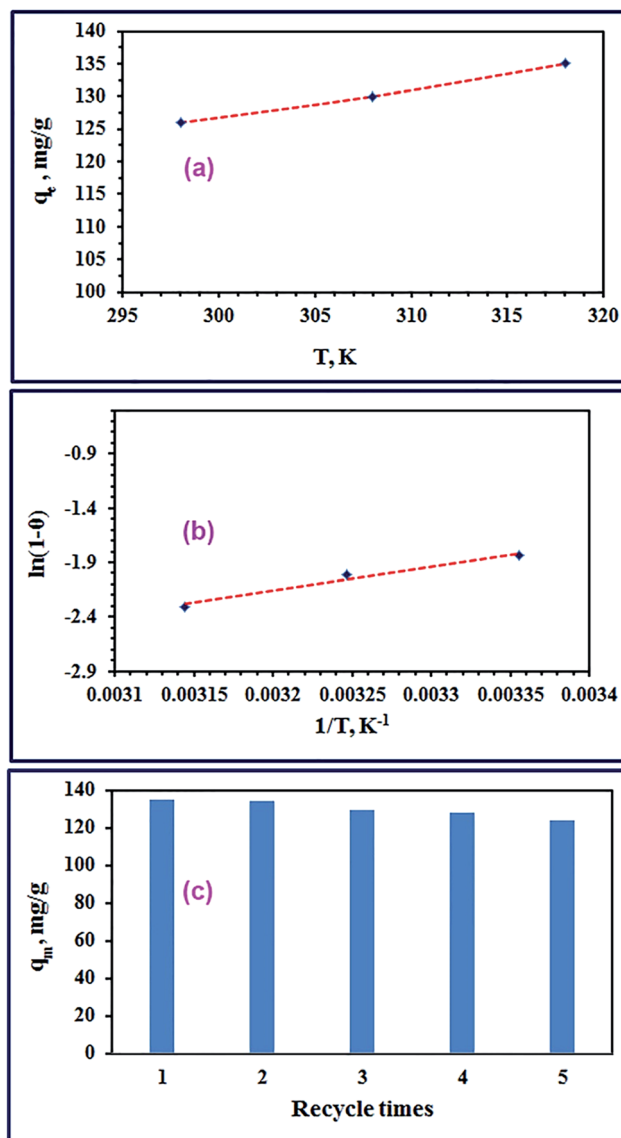| Adsorption isotherm model	Parameters	Value
Langmuir	K_L (L mg^{-1})	0.641
	$q_{m(cal)}$ (mg g^{-1})	127.0
	r_1^2	0.9990
	R_L	0.009941–0.09124
	$q_{e(exp)}$ (mg g^{-1}) at $C_0 = 300$ mg L^{-1}	126.0
Freundlich	K_F [(mg g^{-1}) (L mg^{-1})$^{1/n}$]	50.13
	$q_{m(cal)}$ (mg g^{-1})	167.3
	r_2^2	0.8349
	n	4.732
	$q_{e,(exp)}$ (mg g^{-1}) at $C_0 = 300$ mg L^{-1}	126.0

Fig. 9 Plot of q_e versus T (a), plot of ln$(1 - \theta)$ versus $1/T$ (b), and regeneration efficiency of TiO_2 nano-adsorbent for the removal of RR195 dye (c).

approaches; the partition constant (K_p) and distribution coefficient constant (K_d).[65,70]

As reported by Niwas *et al.* and others,[65] the thermodynamic equilibrium constant (K_c) can be represented by eqn (16).

$$K_c = \frac{a_s}{a_e} = \frac{\gamma_s}{\gamma_e} \frac{C_s}{C_e} \qquad (16)$$

where, a_s and a_e are the activities of the adsorbed dye and the equilibrium dye in solution, respectively. C_s and C_e are the adsorbed concentration of the adsorbate on the adsorbent and the equilibrium concentration of the adsorbate in solutions, respectively. Besides, γ_s and γ_e are the activity coefficients of the adsorbed dye and dye in solution at equilibrium, respectively. When the solute concentration approaches zero in the solution, the activity coefficient approaches unity, and eqn (16) reduces into eqn (17). Therefore the partition coefficient, K_p, equals in its value to the thermodynamic equilibrium constant (K_c), and it is in unison with the thermodynamic constant.

$$K_p = \frac{C_s}{C_e} = \frac{a_s}{a_e} = K_c \qquad (17)$$

The K_p values (*i.e.* $K_c = K_p$ in this case) can be obtained by plotting ln(C_s/C_e) *versus* C_s and extrapolating C_s to zero.[70] The ΔH^0 and ΔS^0 values were estimated from the slope and intercept of the plot of ln K_c against $1/T$. We also calculated ΔG^0 value by feeding ΔH^0 and ΔS^0 values into eqn (14). The calculated thermodynamic parameters are presented in Table (4).

On the other hand, the thermodynamic equilibrium constant was also derived from distribution coefficient constant ($K_d = q_e/C_e$). The distribution coefficient constant (K_d) can be obtained by plotting ln(q_s/C_e) against q_s and extrapolating C_s to zero.[66] Moreover, the thermodynamic equilibrium constant is dimensionless, hence; there is a unit problem with the K_d constant. Therefore, Milonjić proposed that distribution coefficient constant (K_d) can be converted into the dimensionless thermodynamic equilibrium constant (K_c) by multiplying K_d by 1000.[66] The values of ΔH^0 and ΔS^0 were determined from the slope and intercept of the plot of ln K_c against $1/T$. Where, $K_c = K_d \times 1000$. We also estimated ΔG^0 value using eqn (14) by

knowing ΔH^0 and ΔS^0 values. The calculated thermodynamic parameters are tabulated in Table (4). The tabulated thermodynamic values in Table (4) show that the partition coefficient constant is more appropriate than the distribution coefficient for calculating the thermodynamic constants owing to the higher correlation coefficient ($r^2 = 0.9204$) of van't Hoff equation in the case of $K_c = K_p$ on comparing to K_c derived from K_d ($r^2 = 0.786$). It is worthy to mention that both equilibrium constants gave ΔH^0, ΔS^0, and ΔG^0 with same signs.

Based on the thermodynamic parameters calculated from K_c derived from the partition constant, it is indicated that the adsorption process is endothermic and spontaneous due to the positive ΔH^0 and negative ΔG^0 values, respectively, of the process. Besides, increasing the values of ΔG^0 in the negative direction with increasing the temperature indicates the thermodynamic favorability of the adsorption process at higher

Table 4 Thermodynamic constants for the adsorption of RR195 dye on TiO_2 adsorbent from partition and distribution coefficient constants

Method	T (K)	K_c	ΔG^0 (kJ mol^{-1})	ΔS^0 (J mol^{-1} K^{-1})	ΔH^0 (kJ mol^{-1})	r^2	E_a (kJ mol^{-1})	S^*
Partition constant, K_p ($K_p = K_c$)	298	6.498	−4.630	0.02004	1.343	0.9204	18.46	9.464×10^{-5}
	308	6.557	−4.830					
	318	6.725	−5.031					
Distribution coefficient constant, K_d ($K_c = K_d \times 1000$)	298	5805.4	−21.42	0.09113	5.737	0.7860		
	308	5864.2	−22.33					
	318	6725.1	−23.24					

temperatures. Moreover, it could be concluded that the adsorption process of interest was a physisorption process because the ΔG^0 (from −4.630 to −5.031 kJ mol^{-1}) and ΔH^0 (1.343 kJ mol^{-1}) values were in the range of (−20)–(0) kJ mol^{-1} and <40 kJ mol^{-1}, respectively.

In addition, we calculated the activation energy (E_a) of the RR195 dye adsorption on the as-synthesized nano-adsorbent utilizing a modified Arrhenius equation (eqn (18)) related to surface coverage (θ).[71,72]

$$S^* = (1 - \theta)e^{-\frac{E_a}{RT}} \qquad (18)$$

where, S^* ($0 < S^* < 1$) is an adsorbate/adsorbent function (sticking probability), and it is temperature dependent, $\theta = [1 - C_e/C_0]$. C_0 and C_e have the previously mentioned meaning. Substituting of θ with $[1 - C_e/C_0]$ in eqn (18) results in eqn (19)

$$\ln(1 - \theta) = \ln S^* + E_a/RT \qquad (19)$$

We calculated the activation energy (E_a) of the adsorption process from the slope and intercept of the plot $\ln(1 - \theta)$ *versus* $1/T$ (Fig. 9(b)). It is worth mentioning that E_a value can indicate whether the adsorption process is physisorption or chemisorption depending on whether the value lies in the range of 5–40 or 40–800 kJ mol^{-1}, respectively.[4,73] The activation energy (E_a) value of the adsorption of RR195 dye on the as-prepared TiO_2 nano-adsorbent was determined to be 18.46 kJ mol^{-1}. This value indicates the physisorption nature of the adsorption process supporting the previous result concluded from the ΔG^0 and ΔH^0 values.

3.2.6. Effect of the fuels on the adsorption properties of TiO_2 products. We have investigated the influences of combustion fuel and its ratios on the adsorption of the RR195 dye on the calcinated TiO_2 products (A1–U2.5) generated from different fuels. We have applied the following adsorption conditions: 0.05 g TiO_2, 300 mg L^{-1} initial dye concentration, 400 rpm stirring rate, 25 °C temperature, and 120 min contact time. The maximum adsorption capacities of the various TiO_2 products were estimated and tabulated in Table 1. The results listed in Table 1 indicate that urea fuel generated TiO_2 products with the highest adsorption capacities. Moreover, urea fuel with equivalence ratio (Φ_c) values of 0.5 and 1 generated TiO_2 products; U0.5 and U1, with the highest adsorption capacities; 132.0 and 126.0 mg g^{-1}, respectively. However, the TiO_2 product U1 was more separable and handful during the adsorption process on comparing to the U0.5 product; consequently, U1 product

was chosen as the optimum TiO_2 product from the practical point of view.

3.2.7. Reusability of TiO_2 nano-adsorbent and comparison with other adsorbents. The efficiency of the as-prepared TiO_2 nano-adsorbent was investigated by studying its regeneration and reusability for RR195 dye adsorption. Therefore, the adsorption of the dye of interest on the as-prepared TiO_2 nano-adsorbent was achieved under the optimized adsorption conditions; then, we generated the TiO_2 nano-adsorbent by either one of the following two approaches: (i) we extracted the adsorbed RR195 dye employing methanol then the adsorbent was washed with methanol and water. The adsorbent was then dried at about 70 °C for 5 h. (ii) The RR195 dye-loaded TiO_2 adsorbent was ignited at about 450 °C for 0.5 h. We have repeated this recycling procedure five times, and the obtained results are depicted in Fig. 9(c). The results exhibit that the as-prepared TiO_2 product has good reproducibility and high adsorption efficiency even after five cycles of reuse. Moreover, we compared between the maximum adsorption capacity (q_m) of the as-prepared TiO_2 adsorbent with those of others reported in the literature, and the q_m values are presented in Table 5. Additionally, the maximum adsorption capacity (q_m) of the commercially available TiO_2 product (Degussa (P25)) was experimentally determined under the same optimum adsorption conditions, and it was found to be 55.0 mg g^{-1}. We performed this to verify the effectiveness of the as-prepared TiO_2

Table 5 Comparison between the maximum adsorption capacities of various adsorbents toward RR195 dye removal

Adsorbent product	Maximum adsorption capacities, q_m (mg g^{-1})	Reference
Cone biomass	7.38	74
α-Fe$_2$O$_3$	20.5	20
Modified palygorskite with 3-aminopropyl triethoxysilane	34.24	75
Commercial TiO_2 (Degussa (P25))	55.0	Present study
Dehydrated beet pulp carbon	58.0	76
TiO_2	87	53
CoFe$_2$O$_4$	91.7	2
Wheat bran	119.1	77
TiO_2 (U1)	135	Present study
MgO nanoparticles	207	38

product as a potential adsorbent for the removal of RR195 dye. In comparison with the listed q_m of other reported adsorbents (Table 5), it is clear that the as-prepared TiO_2 adsorbent has relatively high q_m values. It is noteworthy that the as-prepared TiO_2 product (U1) has higher adsorption capacity than that of the commercially available TiO_2 (Degussa (P25)). Moreover, MgO adsorbent reported by us elsewhere needed more time and higher temperature in its preparation. Therefore, this comparison and our facile preparation route suggest that the as-synthesized TiO_2 product is a possible promising and applicable candidate in the removal of RR195 dye from aqueous media. The results also indicate the long-term use of the as-prepared TiO_2 adsorbent for the removal of RR195 dye from aqueous solutions.

4. Conclusions

In conclusion, TiO_2 nanostructures were successfully synthesized *via* a facile auto-combustion route using different fuels including L-alanine, glycine, and urea. The results revealed that the fuel type and the fuel-to-oxidant equivalence ratio have a significant influence on the phase, crystallite size, and morphology of the generated TiO_2 products. Urea fuel generated almost the smallest crystallite size (11.9 nm) TiO_2 nanoparticles with single anatase TiO_2 phase at equivalence ratio Φ_c of 1. The as-prepared TiO_2 product generated using urea fuel at $\Phi_c = 1$ showed the highest adsorption capacity (*ca.* 135 mg g^{-1}) for the adsorption removal of RR195 textile anionic dye. In addition, the adsorption results could be well described by the pseudo-second-order and Langmuir adsorption isotherm models. Besides, the contribution into the adsorption mechanism did not arise only from the intra-particle diffusion mechanism but aroused also from the bulk diffusion and film diffusion mechanisms. The adsorption of RR195 dye on TiO_2 nano-adsorbent was a temperature dependent and the process was a physisorption, endothermic, and spontaneous based on the calculated thermodynamic parameters. Moreover, the as-prepared TiO_2 product can be suggested as a promising candidate for the adsorption removal of RR195 dye from aqueous media.

Acknowledgements

References

1 T. A. Khan, S. Dahiya and I. Ali, Use of kaolinite as adsorbent: equilibrium, dynamics and thermodynamic studies on the adsorption of Rhodamine B from aqueous solution, *Appl. Clay Sci.*, 2012, **69**, 58–66.

2 M. Y. Nassar and M. Khatab, Cobalt ferrite nanoparticles *via* a template-free hydrothermal route as an efficient nano-adsorbent for potential textile dye removal, *RSC Adv.*, 2016, **6**, 79688–79705.

3 M. Y. Nassar and S. Abdallah, Facile controllable hydrothermal route for a porous $CoMn_2O_4$ nanostructure: synthesis, characterization, and textile dye removal from aqueous media, *RSC Adv.*, 2016, **6**, 84050–84067.

4 M. Y. Nassar, M. M. Moustafa and M. M. Taha, Hydrothermal tuning of the morphology and particle size of hydrozincite nanoparticles using different counterions to produce nanosized ZnO as an efficient adsorbent for textile dye removal, *RSC Adv.*, 2016, **6**, 42180–42195.

5 N. F. Cardoso, R. B. Pinto, E. C. Lima, T. Calvete, C. V. Amavisca, B. Royer, M. L. Cunha, T. H. M. Fernandes and I. S. Pinto, Removal of remazol black B textile dye from aqueous solution by adsorption, *Desalination*, 2011, **269**, 92–103.

6 B. Kayan, B. Gözmen, M. Demirel and A. M. Gizir, Degradation of acid red 97 dye in aqueous medium using wet oxidation and electro-Fenton techniques, *J. Hazard. Mater.*, 2010, **177**, 95–102.

7 M. Y. Nassar, A. S. Amin, I. S. Ahmed and S. Abdallah, Sphere-like Mn_2O_3 nanoparticles: facile hydrothermal synthesis and adsorption properties, *J. Taiwan Inst. Chem. Eng.*, 2016, **64**, 79–88.

8 M. Y. Nassar, I. S. Ahmed and I. Samir, A novel synthetic route for magnesium aluminate ($MgAl_2O_4$) nanoparticles using sol–gel auto combustion method and their photocatalytic properties, *Spectrochim. Acta, Part A*, 2014, **131**, 329–334.

9 M. Djenouhat, O. Hamdaoui, M. Chiha and M. H. Samar, Ultrasonication-assisted preparation of water-in-oil emulsions and application to the removal of cationic dyes from water by emulsion liquid membrane: part 2. Permeation and stripping, *Sep. Purif. Technol.*, 2008, **63**, 231–238.

10 A. B. Fradj, S. B. Hamouda, H. Ouni, R. Lafi, L. Gzara and A. Hafiane, Removal of methylene blue from aqueous solutions by poly(acrylic acid) and poly(ammonium acrylate) assisted ultrafiltration, *Sep. Purif. Technol.*, 2014, **133**, 76–81.

11 D. Robati, M. Rajabi, O. Moradi, F. Najafi, I. Tyagi, S. Agarwal and V. K. Gupta, Kinetics and thermodynamics of malachite green dye adsorption from aqueous solutions on graphene oxide and reduced graphene oxide, *J. Mol. Liq.*, 2016, **214**, 259–263.

12 E. Pajootan, M. Arami and N. M. Mahmoodi, Binary system dye removal by electrocoagulation from synthetic and real colored wastewaters, *J. Taiwan Inst. Chem. Eng.*, 2012, **43**, 282–290.

13 Q. Wu, W.-T. Li, W.-H. Yu, Y. Li and A.-M. Li, Removal of fluorescent dissolved organic matter in biologically treated textile wastewater by ozonation-biological aerated filter, *J. Taiwan Inst. Chem. Eng.*, 2016, **59**, 359–364.

14 A. Mohammadzadeh, M. Ramezani and A. M. Ghaedi, Synthesis and characterization of Fe_2O_3–ZnO–$ZnFe_2O_4$/carbon nanocomposite and its application to removal of bromophenol blue dye using ultrasonic assisted method: optimization by response surface methodology and genetic algorithm, *J. Taiwan Inst. Chem. Eng.*, 2016, **59**, 275–284.

15 W. Wang, T. Jiao, Q. Zhang, X. Luo, J. Hu, Y. Chen, Q. Peng, X. Yan and B. Li, Hydrothermal synthesis of hierarchical core–shell manganese oxide nanocomposites as efficient dye adsorbents for wastewater treatment, *RSC Adv.*, 2015, **5**, 56279–56285.

16 H. Guo, T. Jiao, Q. Zhang, W. Guo, Q. Peng and X. Yan, Preparation of Graphene Oxide-Based Hydrogels as Efficient Dye Adsorbents for Wastewater Treatment, *Nanoscale Res. Lett.*, 2015, **10**, 1–10.

17 Y. S. Al-Degs, M. I. El-Barghouthi, A. H. El-Sheikh and G. M. Walker, Effect of solution pH, ionic strength, and temperature on adsorption behavior of reactive dyes on activated carbon, *Dyes Pigm.*, 2008, **77**, 16–23.

18 C.-K. Lee, S.-S. Liu, L.-C. Juang, C.-C. Wang, K.-S. Lin and M.-D. Lyu, Application of MCM-41 for dyes removal from wastewater, *J. Hazard. Mater.*, 2007, **147**, 997–1005.

19 A. Nematollahzadeh, A. Shojaei and M. Karimi, Chemically modified organic/inorganic nanoporous composite particles for the adsorption of reactive black 5 from aqueous solution, *React. Funct. Polym.*, 2015, **86**, 7–15.

20 M. Y. Nassar, I. S. Ahmed, T. Y. Mohamed and M. Khatab, A controlled, template-free, and hydrothermal synthesis route to sphere-like [small alpha]-Fe_2O_3 nanostructures for textile dye removal, *RSC Adv.*, 2016, **6**, 20001–20013.

21 M. Y. Nassar and I. S. Ahmed, Template-free hydrothermal derived cobalt oxide nanopowders: synthesis, characterization, and removal of organic dyes, *Mater. Res. Bull.*, 2012, **47**, 2638–2645.

22 A. Razzaz, S. Ghorban, L. Hosayni, M. Irani and M. Aliabadi, Chitosan nanofibers functionalized by TiO_2 nanoparticles for the removal of heavy metal ions, *J. Taiwan Inst. Chem. Eng.*, 2016, **58**, 333–343.

23 S. Yavari, N. M. Mahmodi, P. Teymouri, B. Shahmoradi and A. Maleki, Cobalt ferrite nanoparticles: preparation, characterization and anionic dye removal capability, *J. Taiwan Inst. Chem. Eng.*, 2016, **59**, 320–329.

24 T. Kamal, Y. Anwar, S. B. Khan, M. T. S. Chani and A. M. Asiri, Dye adsorption and bactericidal properties of TiO_2/chitosan coating layer, *Carbohydr. Polym.*, 2016, **148**, 153–160.

25 S. Jafari, B. Tryba, E. Kusiak-Nejman, J. Kapica-Kozar, A. W. Morawski and M. Sillanpää, The role of adsorption in the photocatalytic decomposition of Orange II on carbon-modified TiO_2, *J. Mol. Liq.*, 2016, **220**, 504–512.

26 B. Liu, J. E. Boercker and E. S. Aydil, Oriented single crystalline titanium dioxide nanowires, *Nanotechnology*, 2008, **19**, 505604.

27 N. Erdogan, A. Ozturk and J. Park, Hydrothermal synthesis of 3D TiO_2 nanostructures using nitric acid: characterization and evolution mechanism, *Ceram. Int.*, 2016, **42**, 5985–5994.

28 C. S. Rustomji, C. J. Frandsen, S. Jin and M. J. Tauber, Dye-Sensitized Solar Cell Constructed with Titanium Mesh and 3-D Array of TiO_2 Nanotubes, *J. Phys. Chem. B*, 2010, **114**, 14537–14543.

29 T. Frade, M. E. M. Jorge, B. Fernández, R. Pereiro and A. Gomes, A Possible Growth Mechanism for ZnO–TiO_2 Composite Nanostructured Films Prepared by Electrodeposition, *J. Electrochem. Soc.*, 2014, **161**, D125–D133.

30 Y. Wang, Y. He, Q. Lai and M. Fan, Review of the progress in preparing nano TiO_2: an important environmental engineering material, *J. Environ. Sci.*, 2014, **26**, 2139–2177.

31 K. Ding, Z. Miao, Z. Liu, Z. Zhang, B. Han, G. An, S. Miao and Y. Xie, Facile Synthesis of High Quality TiO_2 Nanocrystals in Ionic Liquid *via* a Microwave-Assisted Process, *J. Am. Chem. Soc.*, 2007, **129**, 6362–6363.

32 L. Mai, C. Huang, D. Wang, Z. Zhang and Y. Wang, Effect of C doping on the structural and optical properties of sol–gel TiO_2 thin films, *Appl. Surf. Sci.*, 2009, **255**, 9285–9289.

33 H. Yoshitake, T. Sugihara and T. Tatsumi, Preparation of Wormhole-like Mesoporous TiO_2 with an Extremely Large Surface Area and Stabilization of Its Surface by Chemical Vapor Deposition, *Chem. Mater.*, 2002, **14**, 1023–1029.

34 A. Daya Mani, B. Rama Raju, N. Xanthopoulos, P. Ghosal, B. Sreedhar and C. Subrahmanyam, Effect of fuels on combustion synthesis of TiO_2 – Towards efficient photocatalysts for methylene blue oxidation and Cr(vi) reduction under natural sunlight, *Chem. Eng. J.*, 2013, **228**, 545–553.

35 A. Daya Mani, V. Laporte, P. Ghosal and C. Subrahmanyam, Combustion synthesized TiO_2 for enhanced photocatalytic activity under the direct sunlight-optimization of titanylnitrate synthesis, *Mater. Res. Bull.*, 2012, **47**, 2415–2421.

36 S. R. Jain, K. C. Adiga and V. R. Pai Verneker, A new approach to thermochemical calculations of condensed fuel-oxidizer mixtures, *Combust. Flame*, 1981, **40**, 71–79.

37 K. C. Patil, Chemistry of Nanocrystalline Oxide Materials: Combustion Synthesis, *Properties and Applications*, World Scientific, 2008.

38 M. Y. Nassar, T. Y. Mohamed, I. S. Ahmed and I. Samir, MgO nanostructure *via* a sol–gel combustion synthesis method using different fuels: an efficient nano-adsorbent for the removal of some anionic textile dyes, *J. Mol. Liq.*, 2017, **225**, 730–740.

39 R. Jenkins and R. L. Snyder, *Introduction to X-ray powder diffractometry*, John Wiley & Sons, Inc., New York, 1996.

40 T. Luttrell, S. Halpegamage, J. Tao, A. Kramer, E. Sutter and M. Batzill, Why is anatase a better photocatalyst than rutile? – Model studies on epitaxial TiO_2 films, *Sci. Rep.*, 2014, **4**, 4043.

41 K. Nakamoto, Infrared and Raman Spectra of Inorganic and Coordination Compounds, *Applications in Coordination, Organometallic, and Bioinorganic Chemistry*, Wiley, 2009.

42 Y. Tang, S. Fu, K. Zhao, G. Xie and L. Teng, Synthesis of TiO_2 nanofibers with adjustable anatase/rutile ratio from Ti sol and rutile nanoparticles for the degradation of pollutants in wastewater, *Ceram. Int.*, 2015, **41**, 13285–13293.

43 S. N. Karthick, K. V. Hemalatha, H. Seo, D. Ludeman, J.-K. Kim, K. Prabakar and H.-J. Kim, Titanium oxide prepared by polymer gel assisted combustion method for dye-sensitized solar cell, *Current Applied Physics*, 2011, **11**, S127–S130.

44 H. M. Aly, M. E. Moustafa, M. Y. Nassar and E. A. Abdelrahman, Synthesis and characterization of novel Cu(II) complexes with 3-substituted-4-amino-5-mercapto-1,2,4-triazole Schiff bases: a new route to CuO nanoparticles, *J. Mol. Struct.*, 2015, **1086**, 223–231.

45 M. Mostafa, H. M. Saber, A. A. El-Sadek and M. Y. Nassar, Preparation and performance of 99Mo/99mTc chromatographic column generator based on zirconium molybdosilicate, *Radiochim. Acta*, 2016, 257–265.

46 M. Y. Nassar, A. S. Attia, K. A. Alfallous and M. F. El-Shahat, Synthesis of two novel dinuclear molybdenum(0) complexes of quinoxaline-2,3-dione: new precursors for preparation of α-MoO$_3$ nanoplates, *Inorg. Chim. Acta*, 2013, **405**, 362–367.

47 M. Y. Nassar, Size-controlled synthesis of CoCO$_3$ and Co$_3$O$_4$ nanoparticles by free-surfactant hydrothermal method, *Mater. Lett.*, 2013, **94**, 112–115.

48 R. Venckatesh, K. Balachandaran and R. Sivaraj, Synthesis and characterization of nano TiO$_2$–SiO$_2$: PVA composite – a novel route, *Int. Nano Lett.*, 2012, **2**, 15.

49 M. Thommes, K. Kaneko, V. Neimark Alexander, P. Olivier James, F. Rodriguez-Reinoso, J. Rouquerol and S. W. Sing Kenneth, Physisorption of gases, with special reference to the evaluation of surface area and pore size distribution (IUPAC Technical Report), *Pure and Applied Chemistry*, 2015, 1051.

50 M. Ahmaruzzaman and S. Laxmi Gayatri, Batch adsorption of 4-nitrophenol by acid activated jute stick char: equilibrium, kinetic and thermodynamic studies, *Chem. Eng. J.*, 2010, **158**, 173–180.

51 M. Kosmulski, pH-dependent surface charging and points of zero charge. IV. Update and new approach, *J. Colloid Interface Sci.*, 2009, **337**, 439–448.

52 E. M. Hotze, T. Phenrat and G. V. Lowry, Nanoparticle Aggregation: Challenges to Understanding Transport and Reactivity in the Environment All rights reserved. No part of this periodical may be reproduced or transmitted in any form or by any means, electronic or mechanical, including photocopying, recording, or any information storage and retrieval system, without permission in writing from the publisher, *J. Environ. Qual.*, 2010, **39**, 1909–1924.

53 V. Belessi, G. Romanos, N. Boukos, D. Lambropoulou and C. Trapalis, Removal of Reactive Red 195 from aqueous solutions by adsorption on the surface of TiO$_2$ nanoparticles, *J. Hazard. Mater.*, 2009, **170**, 836–844.

54 Y. Yang, X. Lin, B. Wei, Y. Zhao and J. Wang, Evaluation of adsorption potential of bamboo biochar for metal-complex dye: equilibrium, kinetics and artificial neural network modeling, *Int. J. Environ. Sci. Technol.*, 2014, **11**, 1093–1100.

55 Y. S. Ho and G. McKay, The sorption of lead(II) ions on peat, *Water Res.*, 1999, **33**, 578–584.

56 Y. S. Ho and G. McKay, Pseudo-second order model for sorption processes, *Process Biochem.*, 1999, **34**, 451–465.

57 F. A. Batzias and D. K. Sidiras, Dye adsorption by prehydrolysed beech sawdust in batch and fixed-bed systems, *Bioresour. Technol.*, 2007, **98**, 1208–1217.

58 W. J. Wber and J. C. Morris, *Proceedings of the International Conference on Water Pollution Symposium*, Pergamon Press, Oxford, New York, 1962.

59 C. Luo, Z. Tian, B. Yang, L. Zhang and S. Yan, Manganese dioxide/iron oxide/acid oxidized multi-walled carbon nanotube magnetic nanocomposite for enhanced hexavalent chromium removal, *Chem. Eng. J.*, 2013, **234**, 256–265.

60 D. Hu and L. Wang, Adsorption of amoxicillin onto quaternized cellulose from flax noil: kinetic, equilibrium and thermodynamic study, *J. Taiwan Inst. Chem. Eng.*, 2016, **64**, 227–234.

61 S. M. Husnain, J.-H. Kim, C.-S. Lee, Y.-Y. Chang, W. Um and Y.-S. Chang, Superparamagnetic nalidixic acid grafted magnetite (Fe$_3$O$_4$/NA) for rapid and efficient mercury removal from water, *RSC Adv.*, 2016, **6**, 35825–35832.

62 G. D. Halsey, The Role of Surface Heterogeneity in Adsorption, in *Advances in Catalysis*, ed. V. I. K. W. G. Frankenburg and E. K. Rideal, Academic Press, 1952, pp. 259–269.

63 T. G. Venkatesha, R. Viswanatha, Y. Arthoba Nayaka and B. K. Chethana, Kinetics and thermodynamics of reactive and vat dyes adsorption on MgO nanoparticles, *Chem. Eng. J.*, 2012, **198–199**, 1–10.

64 Y. Liu, Is the Free Energy Change of Adsorption Correctly Calculated?, *J. Chem. Eng. Data*, 2009, **54**, 1981–1985.

65 R. Niwas, U. Gupta, A. A. Khan and K. G. Varshney, The adsorption of phosphamidon on the surface of styrene supported zirconium(IV) tungstophosphate: a thermodynamic study, *Colloids Surf., A*, 2000, **164**, 115–119.

66 S. K. Milonjić, A consideration of the correct calculation of thermodynamic parameters of adsorption, *J. Serb. Chem. Soc.*, 2007, **72**, 1363–1367.

67 X. Zhou and X. Zhou, The Unit Problem In The Thermodynamic Calculation Of Adsorption Using The Langmuir Equation, *Chem. Eng. Commun.*, 2014, **201**, 1459–1467.

68 P. S. Ghosal and A. K. Gupta, Determination of thermodynamic parameters from Langmuir isotherm constant-revisited, *J. Mol. Liq.*, 2017, **225**, 137–146.

69 H. N. Tran, S.-J. You and H.-P. Chao, Thermodynamic parameters of cadmium adsorption onto orange peel calculated from various methods: a comparison study, *J. Environ. Chem. Eng.*, 2016, **4**, 2671–2682.

70 A. A. Khan and R. P. Singh, Adsorption thermodynamics of carbofuran on Sn(IV) arsenosilicate in H$^+$, Na$^+$ and Ca^{2+} forms, *Colloids Surf.*, 1987, **24**, 33–42.

71 H. R. Mahmoud, S. M. Ibrahim and S. A. El-Molla, Textile dye removal from aqueous solutions using cheap MgO nanomaterials: adsorption kinetics, isotherm studies and thermodynamics, *Adv. Powder Technol.*, 2016, **27**, 223–231.

72 M. Ghaedi, A. Hekmati Jah, S. Khodadoust, R. Sahraei, A. Daneshfar, A. Mihandoost and M. K. Purkait, Cadmium telluride nanoparticles loaded on activated carbon as adsorbent for removal of sunset yellow, *Spectrochim. Acta, Part A*, 2012, **90**, 22–27.

73 J. Ma, Y. Jia, Y. Jing, Y. Yao and J. Sun, Kinetics and thermodynamics of methylene blue adsorption by cobalt–hectorite composite, *Dyes Pigm.*, 2012, **93**, 1441–1446.

74 O. Aksakal and H. Ucun, Equilibrium, kinetic and thermodynamic studies of the biosorption of textile dye (Reactive Red 195) onto *Pinus sylvestris* L., *J. Hazard. Mater.*, 2010, **181**, 666–672.

75 A. Xue, S. Zhou, Y. Zhao, X. Lu and P. Han, Adsorption of reactive dyes from aqueous solution by silylated palygorskite, *Appl. Clay Sci.*, 2010, **48**, 638–640.

76 A. Y. Dursun and O. Tepe, Removal of Chemazol Reactive Red 195 from aqueous solution by dehydrated beet pulp carbon, *J. Hazard. Mater.*, 2011, **194**, 303–311.

77 F. Çiçek, D. Özer, A. Özer and A. Özer, Low cost removal of reactive dyes using wheat bran, *J. Hazard. Mater.*, 2007, **146**, 408–416.